Journal of Alloys and Compounds 509 (2011) 1696–1704

Contents lists available at ScienceDirect

Journal of Alloys and Compounds

journal homepage: www.elsevier.com/locate/jallcom

Effects of heat treatments on microstructure and mechanical properties of Mg–11Y–5Gd–2Zn–0.5Zr (wt.%) alloy

D.D. Yin [a], Q.D. Wang [a,b,*], Y. Gao [a], C.J. Chen [a], J. Zheng [a]

[a] National Engineering Research Center of Light Alloy Net Forming, School of Materials Science and Engineering, Shanghai Jiao Tong University, 800 Dongchuan Road, Shanghai 200240, PR China

[b] The State Key Laboratory of Metal Matrix Composites, School of Materials Science and Engineering, Shanghai Jiao Tong University, 800 Dongchuan Road, Shanghai 200240, PR China

ARTICLE INFO

Article history:
Received 26 July 2010
Received in revised form
28 September 2010
Accepted 29 September 2010
Available online 8 October 2010

Keywords:
Heat-resistant magnesium alloy
Precipitation strengthening
Long period stacking ordered (LPSO)
Slip line
Thermal stability

ABSTRACT

The microstructure and mechanical properties of Mg–11Y–5Gd–2Zn–0.5Zr (wt.%) (WGZ1152) alloy during different heat treatments were investigated. Almost all the $Mg_{24}(GdYZn)_5$ eutectic phases dissolved into the α-Mg matrix after solution treatment at 535 °C for 20 h. After ageing at 225 °C for 24 h (T6 state), a great amount of fine β′ precipitates formed. Both the 18R-type long period stacking ordered (LPSO) $Mg_{12}YZn$ phase and 6H′-type LPSO phase exhibit good thermal stability during the high-temperature heat treatments process. The 18R-type LPSO $Mg_{12}YZn$ phases are much harder than α-Mg matrix and have a volume fraction of ~16%. The ultimate tensile strength at the room temperature of the peak-aged alloy (T6 state) is 307 ± 6 MPa and elongation is 1.4 ± 0.3%. The alloy in T6 state shows anomalous positive temperature dependence of the strength from room temperature to 250 °C, and maintains a strength of more than 260 MPa up to 300 °C (0.64T_m). The excellent strength of the WGZ1152 alloy at both room and elevated temperatures is mainly attributed to the solid solution strengthening, β′ precipitates strengthening and LPSO strengthening. Slip line observations suggest a transition from basal to non-basal slip with increasing temperature.

1. Introduction

As one of the lightest structural metal, Mg alloys have made significant inroads in the aerospace and automotive industries where light weight, consequently, and good fuel economy are essential [1,2]. However the limited high-temperature strength and only average creep resistance of Mg alloys have restricted its wide spread for powertrain applications [3,4].

In the last decade, a mass of efforts have been employed in developing heat-resistant Mg alloys. Anyanwu et al. [5] and He et al. [6] have developed Mg–Gd–Y–Zr alloys which exhibit superior high-temperature properties compared with the conventional Mg alloys and may compete with the commercially available Al alloys. The atomic weight of Y is much less than that of Gd. Therefore adding the same weight of Y can produce higher solubility of alloying elements in matrix, which means higher solid solution strengthening and also higher precipitation hardening can be achieved. On the other hand, it has been reported that Zn addition to Mg–RE (RE = Gd or Y)–(Zr) alloys can cause various novel long period stacking ordered (LPSO) structures [7–11]. These LPSO structures may also play an important role in strengthening Mg alloys.

Bearing in mind the above mentioned facts, a new Mg–11Y–5Gd–2Zn–0.5Zr (wt.%) (WGZ1152) alloy has been developed. It exhibits great potential for powertrain applications. Our previous works have investigated its thermal properties [12] and microstructure in the as-cast state [8]. However, the effects of heat treatments on microstructure and mechanical properties have yet to be studied.

The aim of this work is to investigate the microstructure and mechanical properties during heat treatments, and the relationship between microstructure and mechanical properties is also discussed.

2. Experimental procedures

Actual composition of the studied alloy was Mg–11.3Y–4.7Gd–2.0Zn–0.46Zr (wt.%). It was prepared from high purity (≥99.9%) Mg, Zn and Mg–25Y (wt.%), Mg–25Gd (wt.%) and Mg–30Zr (wt.%) master alloys by induction melting in a mild steel crucible at approximate 750 °C under protection of a mixed atmosphere of CO_2 and SF_6 with the ratio of 100:1 and then the melt was poured into a steel mould pre-heated to 200 °C. The actual chemical composition of the alloy was determined by an inductively coupled plasma (ICP) analyzer. The alloy was solution treated at 535 °C for 20 h under the SO_2 atmosphere, and then quenched into cold water. After solution treatment, the alloy was isothermally aged at 225, 250 and 300 °C for different times in an oil bath furnace. The ageing response of the alloy was measured by

* Corresponding author at: National Engineering Research Center of Light Alloys Net Forming and State Key Laboratory of Metal Matrix Composites, School of Materials Science and Engineering, Shanghai Jiao Tong University, 800 Dongchuan Road, Shanghai 200240, PR China. Tel.: +86 21 54742715; fax: +86 21 34202794.
E-mail address: wangqudong@sjtu.edu.cn (Q.D. Wang).

0925-8388/$ – see front matter © 2010 Elsevier B.V. All rights reserved.
doi:10.1016/j.jallcom.2010.09.194

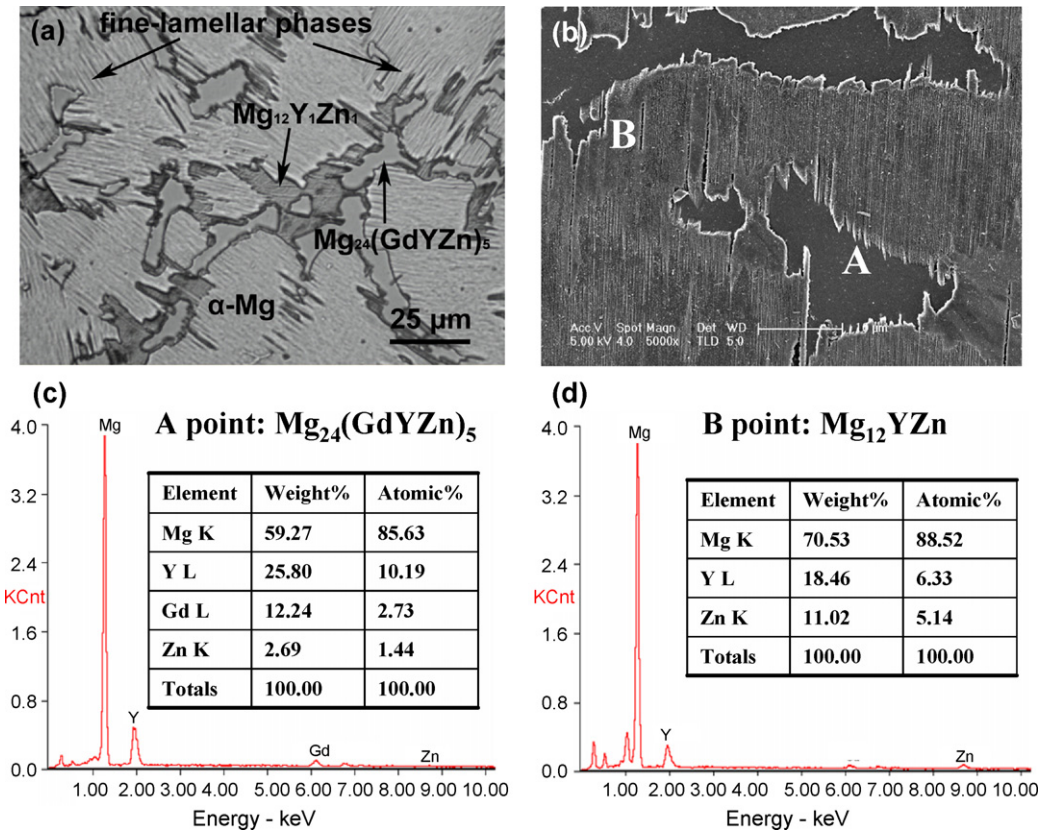

Fig. 1. Microstructure of the as-cast WGZ1152 alloy: (a) optical micrograph, (b) SEM micrograph, (c) and (d) corresponding EDS results of the points indicated in (b).

Vickers hardness tester under 49 N load and a hold time of 15 s. The microhardness of phases in the alloy was measured by a Vickers microhardness tester under 50 gf load and hold time of 30 s.

Rectangular tensile specimens, 3.5 mm in width, 2 mm in thickness and 15 mm in gauge length, were cut from the ingot using electric sparking technique. The tensile tests were carried out on Shimadzu machine at temperature range from 25 to 300 °C with strain rate of 1×10^{-3} s^{-1}. Each test condition was repeated at least three times for repeatability and accuracy.

Microstructure examinations were performed using an optical microscope (LEICA MEF4M), scanning electron microscope (FEI SIRION 200) equipped with an Oxford INCA energy dispersive X-ray spectrometer and transmission electron microscopes (Philips CM20 and JEM-2010) operated at 200 kV. Specimens for slip lines observations were first carefully mechanical polished, then etched in a 4 vol.% natal. The grain size was determined using a linear intercept method [13] ($D = 1.5l$, D is mean grain diameter, l is mean linear intercept) from a large number of measurements. The mean diameter and volume fraction of phases in the alloy were determined using a quantitative metallographic method by image analysis software (Image-Pro Plus 6.0) from at least 10 optical micrographs (100 or 400×) for each heat treatment conditions of the alloy.

3. Results

3.1. Microstructure

3.1.1. Microstructure of the as-cast alloy

The optical and SEM micrographs with corresponding EDS results of the as-cast Mg–11Y–5Gd–2Zn–0.5Zr (wt.%) (WGZ1152) alloy are shown in Fig. 1. The average grain size of the as-cast alloy is 51 ± 9 μm. As seen from Fig. 1(a), the as-cast alloy mainly consists of four phases, which are fine-lamellar phase, network-shaped grayish phase, strip-shaped black phase and the α-Mg matrix. XRD analysis [Fig. 2(a)] and EDS results [Fig. 1(c) and (d)] indicate that the network-shaped phase is the $Mg_{24}(GdYZn)_5$ eutectic compound, and the network-shaped black phase is $Mg_{12}YZn$ compound. The $Mg_{24}(GdYZn)_5$ and $Mg_{12}YZn$ phases are both distributed along the grain boundaries. The fine-lamellar phases are uniformly distributed from grain boundaries to the interior of the α-Mg grains and are orientated in one direction within a grain. This suggests that fine-lamellar phases have a specific orientation relationship with the α-Mg matrix. Our previous work has shown that the fine-lamellar phases have a 6H′-type (ABCBCB′) LPSO structure [8]. Fig. 3(a) shows a SEM micrograph of the $Mg_{12}YZn$ phases distributed along the grain boundaries in the as-cast alloy. It appears that the strip-shaped $Mg_{12}YZn$ phases are coarsened by the fine-lamellar $Mg_{12}YZn$ aggregating. Fig. 3(b) and (c) show a TEM micrograph of the $Mg_{12}YZn$ phases with a corresponding selected area diffraction pattern (SADP). As shown in the micrograph, the

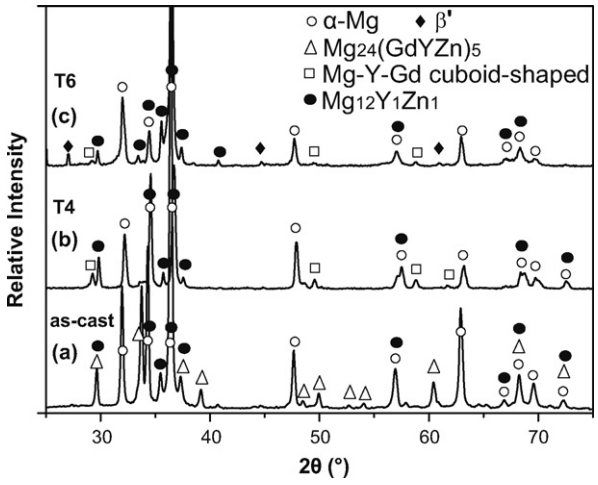

Fig. 2. XRD patterns of WGZ1152 alloy in different states: (a) as-cast, (b) T4: solution treated at 535 °C for 20 h, (c) T6: solution treated at 535 °C for 20 h and then aged at 225 °C for 24 h.

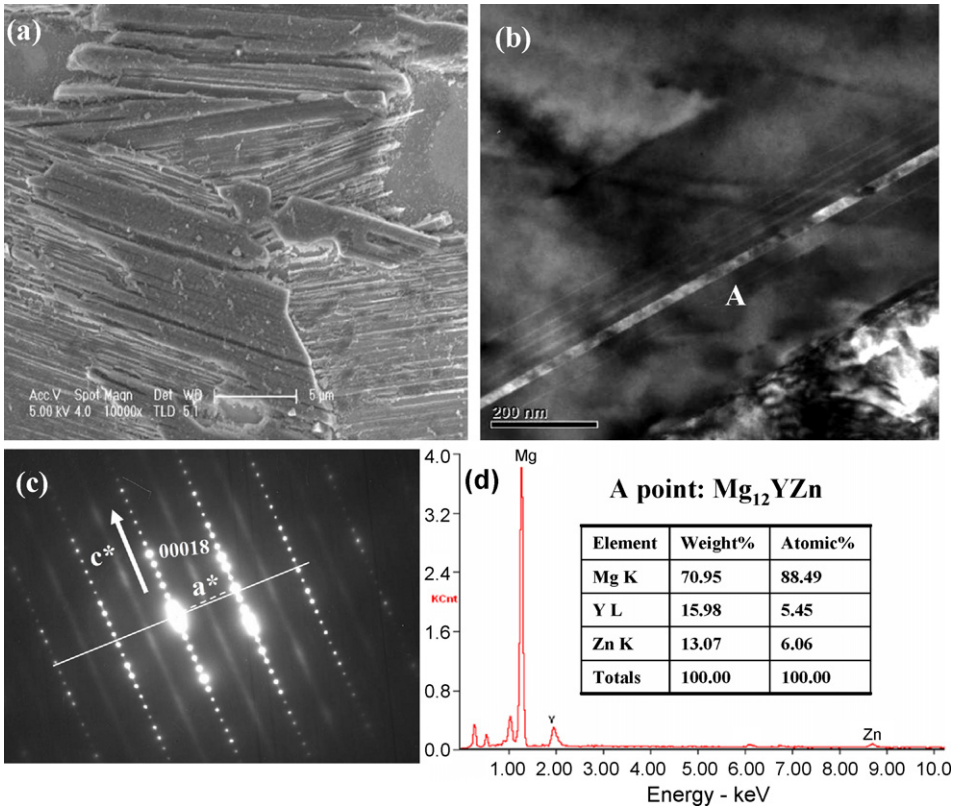

Fig. 3. (a) SEM micrograph of the $Mg_{12}YZn$ phases distributed along the grain boundaries in the as-cast WGZ1152 alloy. (b) TEM micrograph of the $Mg_{12}YZn$ phases with (c) SADP taken from area A in the as-cast alloy. Note that extra reflection spots appear in the SADP indicating an 18R-type LPSO structure and the solid line is perpendicular to *c*-axis. (d) Corresponding EDS results of point A indicated in (b).

Table 1
The mean diameter and volume fraction of the second phases in different states of WGZ1152 alloy.

Phase	F		T4		T6	
	Mean diameter (μm)	Volume fraction (%)	Mean diameter (μm)	Volume fraction (%)	Mean diameter (μm)	Volume fraction (%)
$Mg_{12}YZn$	12.9 ± 8.1	14.3 ± 2.8	7.7 ± 5.2	17.0 ± 2.4	7.2 ± 4.9	16.1 ± 2.7
Cuboid-shaped			3.7 ± 1.2	1.2 ± 0.1	3.7 ± 2.6	2.1 ± 0.3
$Mg_{24}(GdYZn)_5$	25.7 ± 18.3	9.5 ± 1.1				

Note: F: as-cast; T4: solution treated at 535 °C for 20 h; T6: solution treated at 535 °C for 20 h and aged at 225 °C for 24 h.

$Mg_{12}YZn$ also shows fine-lamellar contrasts. The extra reflection spots appearing in the SADP indicate that $Mg_{12}YZn$ phase has an 18R-type LPSO structure [11,14,15] Corresponding EDS results (Fig. 3(d)) show that the average chemical composition of the LPSO phase is Mg–6Y–5Zn (at.%), confirming that it is the $Mg_{12}YZn$. Luo and co-workers [15,16] have identified this LPSO phase is the 18R-type (ACBCBCBACACACBABAB) structure with a period of 0.26 nm.

As seen in Table 1, the mean diameter and the volume fraction of $Mg_{12}YZn$ phases in the as-cast alloy are 12.9 ± 8.1 μm and 14.3 ± 2.8%, respectively, while for $Mg_{24}(GdYZn)_5$ eutectic phase they are 25.7 ± 18.3 μm and 9.5 ± 1.1%.

Fig. 4 illustrates the DTA trace of the as-cast alloy during heating. The first peak may correspond with the melting of the $Mg_{24}(GdYZn)_5$ eutectic phase. The second peak may be related to the melting of the alloy. The eutectic temperature and melting point are evaluated to be approximately 535 and 628 °C, respectively.

3.1.2. Microstructure of the solution-treated alloy

Fig. 5(a) presents an optical micrograph of the alloy after solution treatment at 535 °C for 20 h. The average grain size of the solution-treated alloy is 108 ± 14 μm. Almost all the $Mg_{24}(GdYZn)_5$ eutectic phases have dissolved into the α-Mg matrix, while the $Mg_{12}YZn$ phases remained at the grain boundaries [also confirmed by the XRD analysis in Fig. 2(b)]. The mean diameter and volume fraction of the $Mg_{12}YZn$ phases in the solution-treated alloy are 7.7 ± 5.2 μm and 17.0 ± 2.4%, respectively (Table 1).

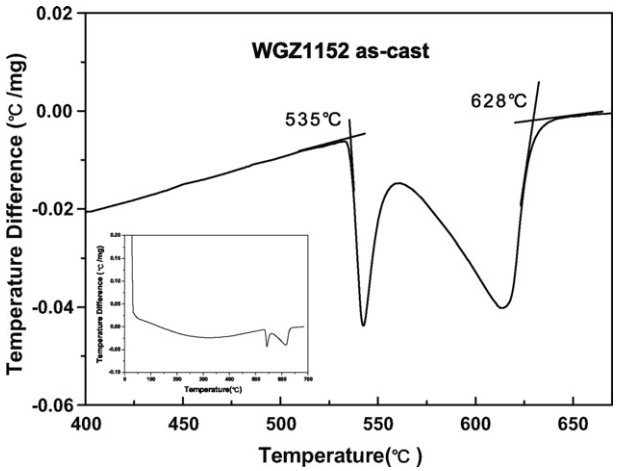

Fig. 4. DTA trace of the as-cast WGZ1152 alloy.

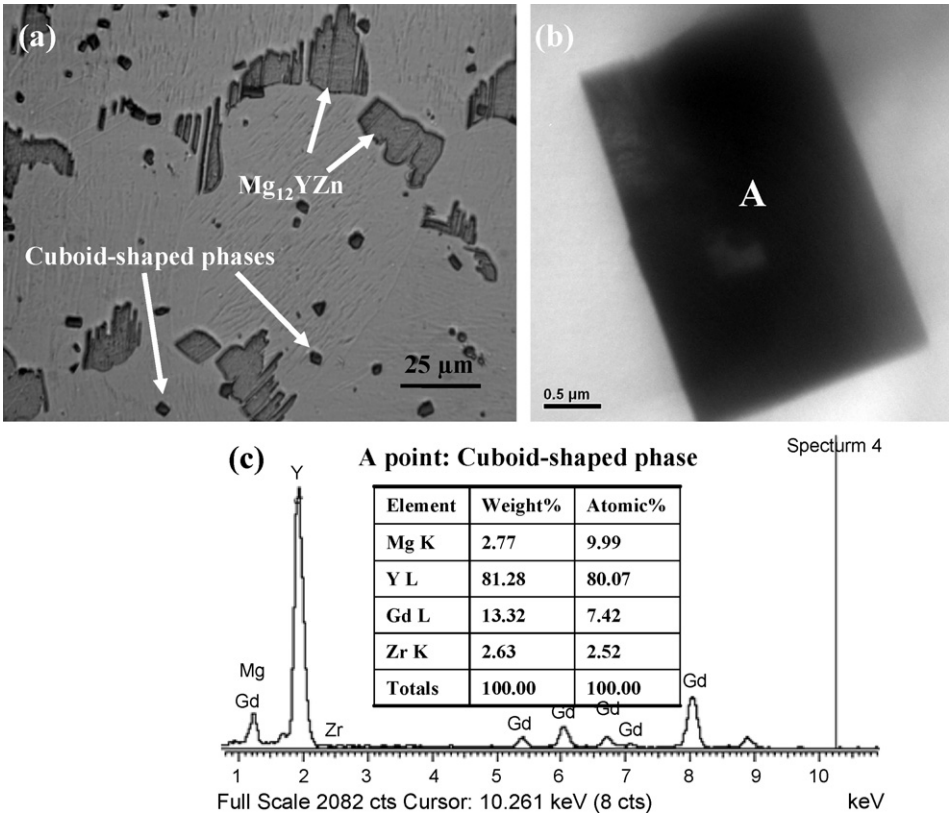

Fig. 5. (a) Optical micrograph of WGZ1152 alloy after solution treated at 535 °C for 20 h. (b) TEM micrograph of cuboid-shaped phase in the solution-treated alloy and (c) corresponding EDS results of point A indicated in (b).

As seen from Fig. 5(a), some cuboid-shaped phases appeared after solution treatment and were distributed randomly at the grain boundaries or within the grains. This means the new phases are mainly generated during solution treatment. The mean diameter and volume fraction of the cuboid-shaped phases are 3.7 ± 1.2 μm and 1.2 ± 0.1%, respectively (Table 1). Fig. 5(b) shows a TEM micrograph of the cuboid-shaped phases. The corresponding EDS results [Fig. 5(c)] indicate they are rich in Y, Gd and Zr.

Fig. 6 shows a TEM micrograph and corresponding SADP of the fine-lamellar phases in the solution-treated alloy. The beam direction was approximately parallel to $[2\bar{1}\bar{1}0]$ zone axis. Periodic streaks with a distance of 1.54 nm $\approx 6 \times d_{(0002)Mg}$ are observed in Fig. 6(a), as indicated by the arrows. The extra reflection spots in the SADP [Fig. 6(b)] indicate a 6H′-type LPSO structure in the phases [7,8,14]. Note that the *c*-axis is not perpendicular to the *a*-axis and the angle between them is about 88°, as indicated in Fig. 6(b). The fine-lamellar phases with 6H′-type LPSO structure in the solution-treated alloy is considered to be the same phases as the fine-lamellar phases observed in the as-cast alloy, reported by Gao et al. [8].

3.1.3. Microstructure of the aged alloy

The optical micrographs in different ageing states are shown in Fig. 7. The average grain sizes of the alloys after ageing at 225 and

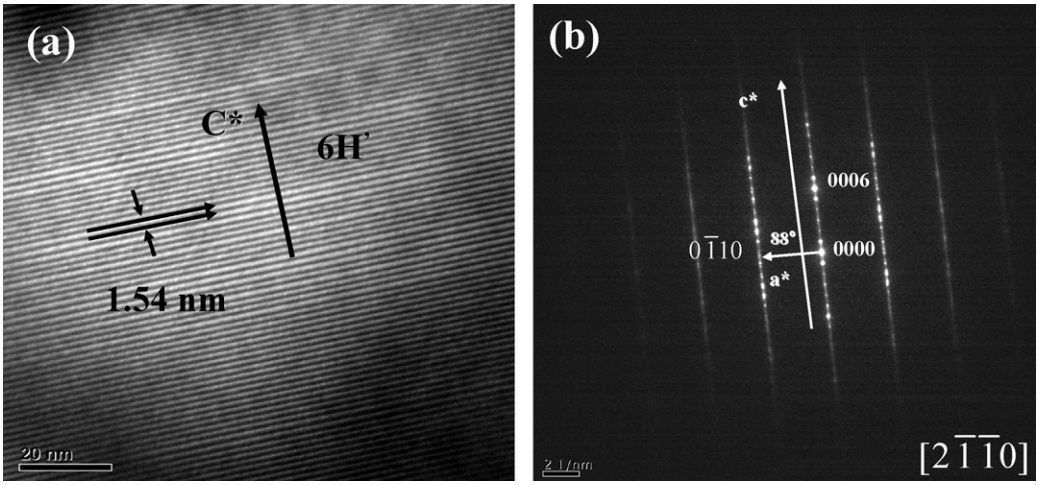

Fig. 6. (a) TEM micrograph of the fine-lamellar phases in solution-treated WGZ1152 alloy and (b) SADP of the fine-lamellar phases, extra reflection spots indicate a 6H′-type (ABCBCB′) LPSO structure in the fine-lamellar phases. The beam direction is approximately parallel to $[2\bar{1}\bar{1}0]$ zone axis.

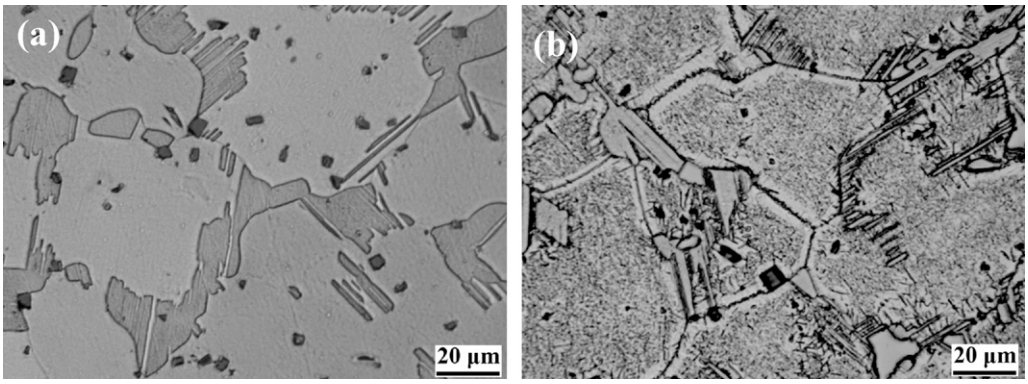

Fig. 7. Optical micrographs of WGZ1152 alloy after solution treated at 535 °C for 20 h and aged (a) at 225 °C for 24 h, (b) at 300 °C for 24 h.

300 °C for 24 h are 116 ± 15 and 120 ± 20 μm, respectively. No obvious grain growth was observed after ageing. XRD analysis [Fig. 2(c)] and optical micrograph show that the morphology and amount of the $Mg_{12}YZn$ phases and cuboid-shaped phases in the aged alloy are almost identical to that of the solution-treated alloy [Fig. 5(a)]. The mean diameter and volume fraction of the $Mg_{12}YZn$ phases in the alloy after ageing at 225 °C for 24 h are 7.2 ± 4.9 μm and 16.1 ± 2.7%, respectively (Table 1). While for cuboid-shaped phases they are 3.7 ± 2.6 μm and 2.1 ± 0.3%, respectively (Table 1).

After ageing at 225 °C for 24 h, some small peaks marked "♦" appeared in the XRD pattern [Fig. 2(c)]. This suggests that some new precipitates formed in the aged alloy. Fig. 8 shows TEM micrographs and SADPs of precipitates within grains after ageing at 225 °C for 24 h. As seen in the micrographs, the dense spheroidal precipitates with a diameter about 5–40 nm are evenly dispersed in the matrix. The SADPs [Fig. 8(c) and (d)] taken from the [0 0 0 1] and [2 $\bar{1}$ $\bar{1}$ 0] zone axis, respectively, indicate that the precipitates are β′ phases and the orientation relationship between the β′ phases and α matrix is: $(100)_{\beta'}//(1\bar{2}10)_{\alpha}$, $[0001]_{\beta'}//[0001]_{\alpha}$ [6,17,18]. Its structure was identified as an orthorhombic (cbco, $a = 2 \times a_{Mg} = 0.640$ nm, $b = 8 \times d_{10\bar{1}0Mg} = 2.223$ nm, $c = c_{Mg} = 0.521$ nm) [17]. Fig. 9(a) shows the fine-lamellar phases and β′ precipitates coexist in the alloy after ageing at 225 °C for 24 h. A SADP [Fig. 9(b)] taken from the fine-

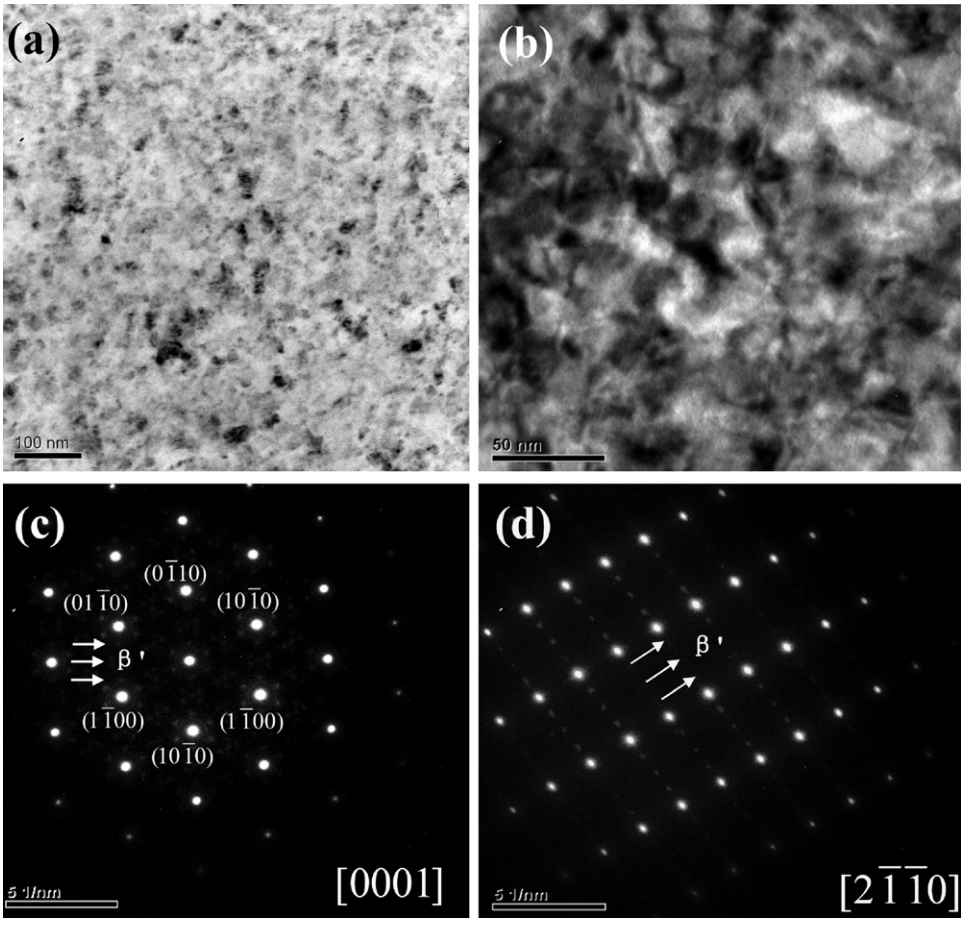

Fig. 8. TEM micrographs and SADPs of the β′ precipitates in WGZ1152 alloy after solution treated at 535 °C for 20 h and aged at 225 °C for 24 h. The beam direction is approximately parallel to (c) [0 0 0 1] zone axis and (d) [2 $\bar{1}$ $\bar{1}$ 0] zone axis.

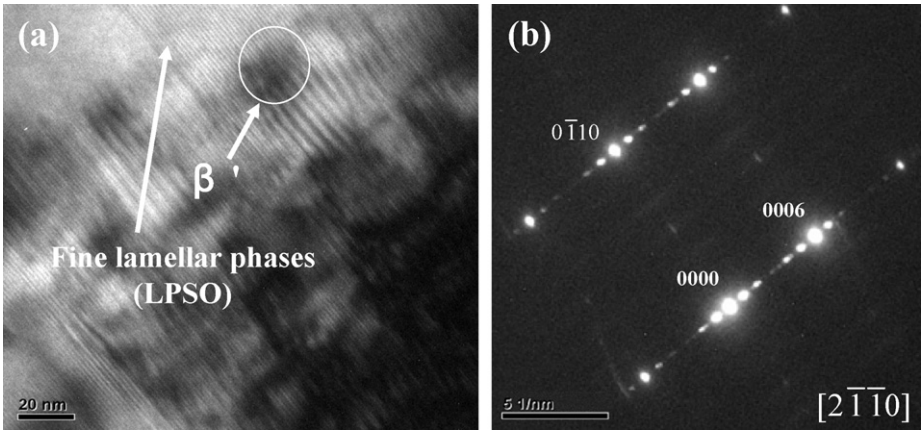

Fig. 9. (a) TEM micrograph of the fine-lamellar phases and the β′ precipitates in WGZ1152 alloy after solution treated at 535 °C for 20 h and aged at 225 °C for 24 h. (b) SADP of the fine-lamellar phases in (a), indicating its structure is still a 6H′-type (ABCBCB′) LPSO. The beam direction is approximately parallel to [2 1 1 0] zone axis.

lamellar phases region in the aged alloy indicates a 6H′-type LPSO structure of the fine-lamellar phases. These fine-lamellar phases are considered to be the same phases as are those in the as-cast and solution-treated alloy mentioned before (Sections 3.1.1 and 3.1.2).

After ageing at 300 °C for 24 h, coarse plate-shaped precipitates with a length of 0.3–1 μm and a width of 50–200 nm formed (Fig. 10). The corresponding SADP indicates that the precipitates are β phases, which have an f.c.c. crystal structure (a = 2.2 nm) and the orientation relationship between β and α matrix is $(\bar{1}\,1\,2)_\beta//(1\,\bar{1}\,0\,0)_\alpha$, $[1\,1\,0]_\beta//[0\,0\,0\,1]_\alpha$ [17,18].

3.2. Mechanical properties

3.2.1. Ageing hardening response

Fig. 11 shows the ageing hardening response for the alloy aged at 225, 250, 300 °C. Before ageing, the specimens were solution treated at 535 °C for 20 h. It exhibits decrease of the maximum hardness with increasing ageing temperature from 225 to 300 °C. Moreover, with the increasing ageing temperature it takes almost the same time to reach the maximum hardness for all three levels of the ageing temperature. All the specimens show a wide peak hardness plateau from about 20–24 to 126 h. The specimen aged at 225 °C shows the strongest hardening response with a maximum value of 137 HV being obtained after 24 h.

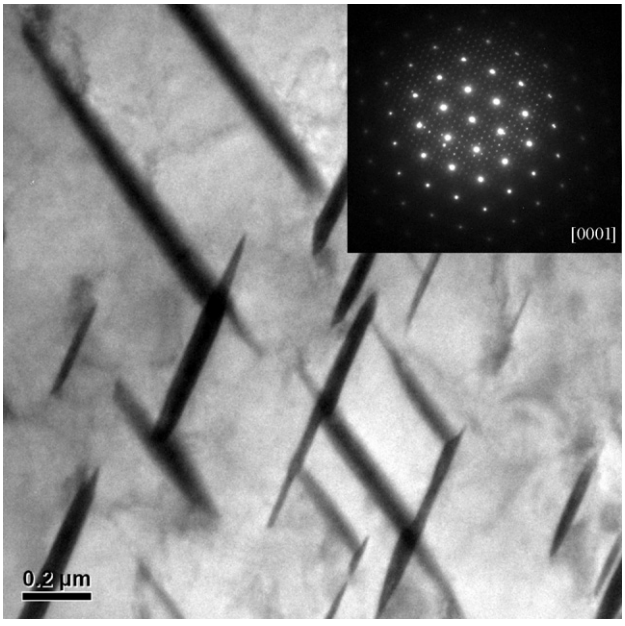

Fig. 10. TEM micrograph and corresponding SADP of the β precipitates in WGZ1152 alloy after solution treated at 535 °C for 20 h and aged at 300 °C for 24 h. The beam direction is approximately parallel to [0 0 0 1] zone axis.

3.2.2. Microhardness

Fig. 12 exhibits the microhardness of phases in different states of the WGZ1152 alloy: F: as-cast; T4: solution treated at 535 °C for 20 h; T6: solution treated at 535 °C for 20 h and aged at 225 °C for 24 h. For the α-Mg matrix, the T6 specimen exhibits the highest microhardness (128.0 ± 6.9 HV) while the T4 specimen shows the lowest (75.9 ± 8.8 HV). The $Mg_{24}(GdYZn)_5$ eutectic phase, which only appears in the as-cast alloy, exhibits a microhardness of 146.4 ± 5.4 HV. Meanwhile the 18R-type LPSO $Mg_{12}YZn$ phase, which remains nearly unchanged in all three states of the alloy, exhibits the highest microhardness (161.0 ± 10.3 HV) compared with the other phases examined.

3.2.3. Temperature dependence of tensile properties

Fig. 13 illustrates the temperature dependence of tensile properties of the alloy in different states: F: as-cast; T4: solution treated at 535 °C for 20 h; T6: solution treated at 535 °C for 20 h and aged at 225 °C for 24 h. At room temperature, a noticeable improvement of ultimate tensile strength (UTS) was observed from both F to T4 and T4 to T6 state, by about 43% (76 MPa) and 21% (54 MPa), respectively. Meanwhile the elongation to failure is greatly increased by

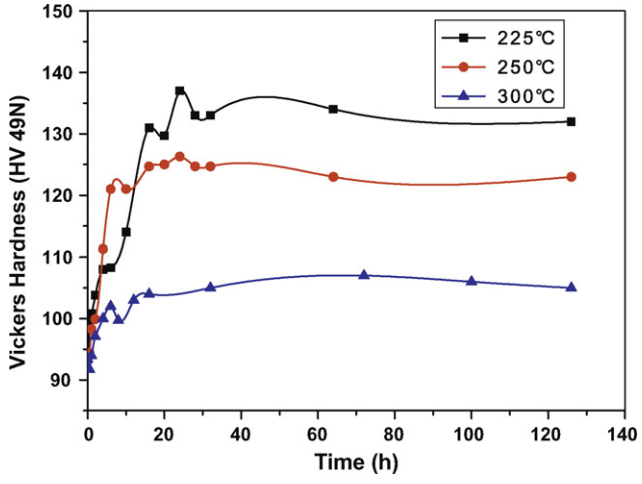

Fig. 11. Ageing hardening response at 225, 250 and 300 °C of WGZ1152 alloy.

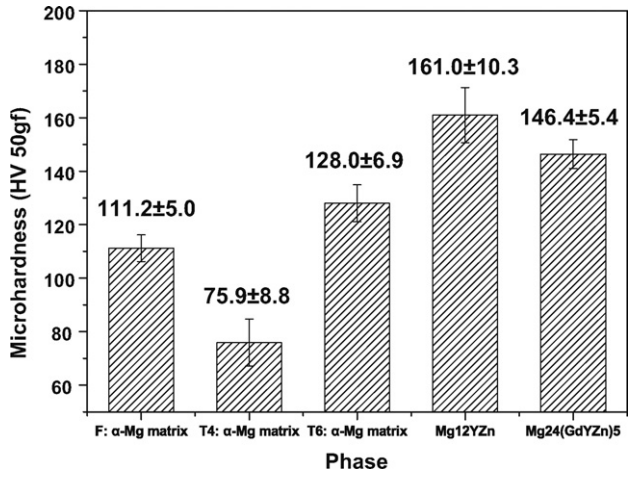

Fig. 12. Microhardness of phases in WGZ1152 alloy for different states: F: as-cast; T4: solution treated at 535 °C for 20 h; T6: solution treated at 535 °C for 20 h and aged at 225 °C for 24 h.

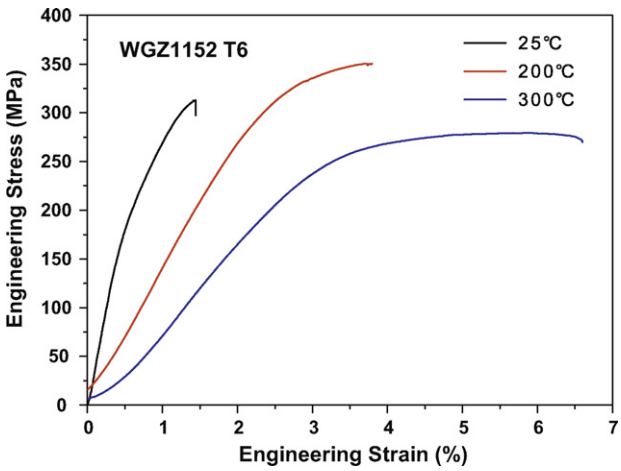

Fig. 14. Temperature dependence of the engineering stress–strain curves for peak-aged WGZ1152 alloy. T6 state: solution treated at 535 °C for 20 h and aged at 225 °C for 24 h.

approximately five times from F (~0.6%) to T4 (~3%) state. After ageing, the elongation to failure is reduced from ~3% to ~1.4%, compared with that in T4 state.

As seen from Fig. 13, the alloy in T6 state exhibits the highest strength over the temperature range of 25–300 °C while the alloy in F state shows the lowest strength. But at 300 °C, the strength of the alloy in T6 state steeply decreases, and the difference in strength between the T6 and T4 states becomes small. In addition, both F and T6 specimens exhibit anomalous positive temperature dependence of strength while the strength of T4 specimen decline slightly with temperature increasing from 25 to 300 °C. On the other hand, the elongation to failure of the T4 and T6 specimens remarkably increases while the tensile strength sharply decreases. The elongation to failure of the T4 specimen is larger than that of the F and T6 specimens, especially at 100 °C and above. The elongation to failure of all the three states increases with increasing temperature. Note that the alloy in F state has the smallest increase of elongation. It should be mentioned that the alloy in T6 state exhibits a strength of more than 300 MPa and an elongation to failure of ~5% at 250 °C ($0.58T_m$). Moreover, even at temperature as high as 300 °C ($0.64T_m$), the alloy in T6 state to exhibits a strength of ~266 MPa.

Fig. 14 illustrates typical engineering stress–strain curves for the alloy in T6 state. The stress increases to a maximum value and then decreases to final rupture. The strength and elongation to failure improve simultaneously from room temperature to 200 °C. At 300 °C, a steady state flow stress with little softening is observed. Slip lines near the tensile fractured area at various temperatures (T6 state) are exhibited in Fig. 15. At 100 °C basal slip is dominant, as indicted by the long straight lines in Fig. 15(a); At 250 °C, extensive non-basal slip and cross-slip associated with short wavy slip traces are observed [Fig. 15(b) and (c)]; Extensive multiple slip are found at 300 °C [Fig. 15(d)]. These surface observations suggested a transition from basal to non-basal slip with increasing temperature [19].

4. Discussion

The optimal solution parameter of 535 °C for 20 h was chosen for WGZ1152 alloy according to literature data [20,21] and the DTA trace (Fig. 4). After solution treated, the $Mg_{24}(GdYZn)_5$ eutectic phases dissolved into the α-Mg matrix and the alloying elements Y and Gd homogenously distributed throughout the grains. Elongation to failure greatly increased for the dissolution of $Mg_{24}(GdYZn)_5$ eutectic phases and homogenous distribution of alloying elements, and UTS also enhanced remarkably due to the solution strengthening of Y and Gd.

Some cuboid-shaped and RE enriched phases appeared after solution treated, indicating they are mainly formed during the solution treatment. Similar cuboid-shaped phases have been found in many solution treated Mg–RE (Y, Gd and Sm)–Zr alloys [6,20–22]. The f.c.c. crystal structure with $a \approx 0.56$ nm was determined by He

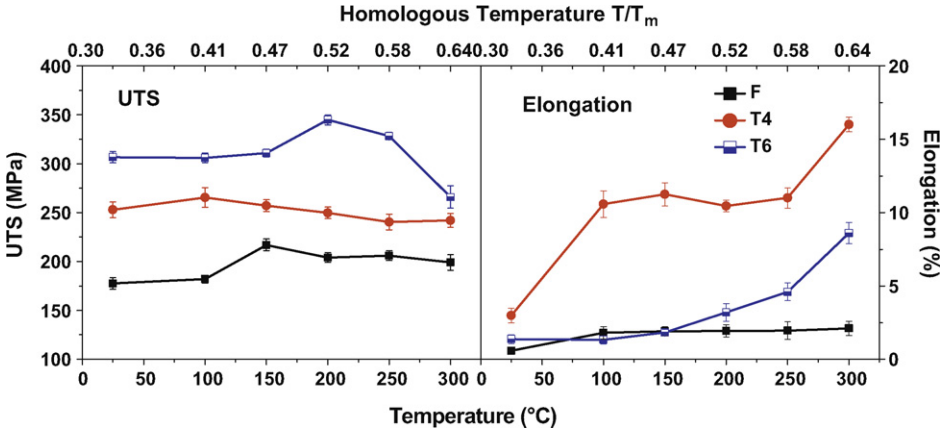

Fig. 13. Tensile properties of different states of WGZ1152 alloy at room temperature and elevated temperatures. F: as-cast; T4: solution treated at 535 °C for 20 h; T6: solution treated at 535 °C for 20 h and aged at 225 °C for 24 h.

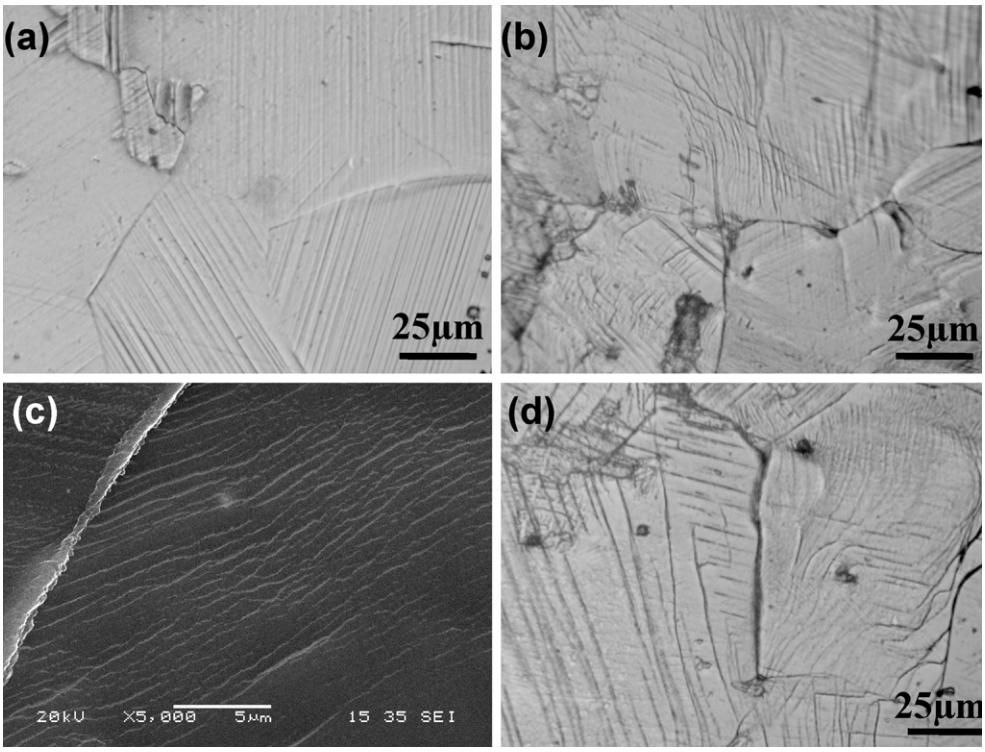

Fig. 15. Optical and SEM micrographs near the tensile fractured area, showing the slip lines. (a) $T = 100\,^{\circ}C$, long straight lines of basal slip; (b), (c) $T = 250\,^{\circ}C$, short wavy slip traces of non-basal slip and cross slip; (d) $T = 300\,^{\circ}C$, extensive multiple slip (T6 state: solution treated at 535 °C for 20 h and aged at 225 °C for 24 h).

et al. [6] but the composition varied due to the different alloying elements. What is more, they almost do not change (Table 1) in the subsequent ageing process (225 °C for 24 h), indicating this phase has relatively good thermal stability. The relatively large size and small volume fraction of the phases may have only small strengthening contributions. The exact effects of the cuboid-shaped phases on the mechanical properties of the alloy remain unclear and are still under studying.

Ageing temperature and time are two of the most important factors influencing the mechanical properties of the alloy. After ageing at 225 °C for 24 h, the highest hardness (~137 HV) was obtained. However, when aged at 300 °C for the same time, the peak hardness decreased by ~45 HV. Note that there was no obvious grain growth (~120 μm), so the decline of hardness can be explained exclusively by the transformation from fine β′ precipitates to coarse β precipitates.

Generally speaking, the alloy containing fine, shear-resistant, evenly oriented (the planes parallel to the prismatic or basal planes of Mg matrix) and uniformly distributed particles, with adequate volume fraction, can exhibit a very high strength [10,13]. In the case of the alloy in T6 state (aged at 225 °C for 24 h), the fine, dense and uniformly dispersed β′ phases are the main precipitates (Fig. 8). It has been reported that β′ precipitates, which form on the prismatic planes of α-Mg matrix in a dense triangular arrangement [6], are perpendicular to the basal plane of α-Mg and stable at 250 °C [18]. This precipitates have great ability to retard dislocation motion on the basal planes [23]. However, this prismatic precipitates are thought to be less effective obstacles to non-basal slip or cross slip [6]. Meanwhile, slip line observations reveal a transition from basal slip to non-basal slip with increasing temperature and extensive multiple slip occurring at 300 °C (Fig. 15). Therefore, it can explain why the strength of the alloy in T6 state is high at lower temperatures, while at a higher temperature of 300 °C, its strength sharply decreases and the elongation increases remarkably.

At elevated temperatures, the grain boundary function as sites of weakness and grain-boundary sliding becomes an additional deformation mechanism [13]. The $Mg_{12}YZn$ phase, which is densely distributed in the matrix and along the grain boundaries (volume fraction is ~16%, Table 1), is hard (microhardness is 26%, 112% and 45% higher than that of T6, T4 and F α-Mg matrix, respectively, Fig. 12) and also thermally stable (almost no change during the process of high-temperature heat treatment, Table 1). This phase is believed to be able to pin the grain-boundary sliding and strengthen the boundaries effectively, especially at elevated temperatures.

It should be noted that in this alloy there are two types of LPSO phases, namely the 18R-type LPSO in $Mg_{12}YZn$ phase and 6H′-type LPSO phase within the α-Mg matrix. Both of them are formed in the conventional cast process, and remain stable during the subsequent high-temperature heat treatments. This indicates that the two LPSO phases in WGZ1152 alloy have a good thermal stability. Although this work only examined the microhardness of one type of LPSO phase (18R-type LPSO $Mg_{12}YZn$ phase), which exhibits a much higher microhardness than the α-Mg matrix, it is reasonable to believe that both LPSO phases in the alloy have high microhardness. Chino et al. [9] and Itoi et al. [11] using nano-indentation test have proved the 6H-type and 18R-type LPSO phase have high hardness and elastic modulus in Mg–Y–Zn alloy, respectively.

At elevated temperatures, non-basal slip is activated (Fig. 15) and may become an important deformation process [13,19]. Matsuda et al. [10] have reported that the critical resolved shear stress of the basal plane increases by the formation of the LPSO phase. Thus the LPSO phase can contribute to strengthening. On the other hand, the LPSO phase is not only a long-period stacking-ordered but also chemical-ordered structure [7]. It is reported that in ordered structure the dislocations must travel in pairs—a leading dislocation and a trailing dislocation, and the dislocations in pairs can hardly climb or cross-slip [24]. Therefore, the high-temperature strength can be increased significantly. Based on above analysis, it is rea-

sonable to believe that the hard, ductile [11] and thermally stable LPSO phases provide important strengthening sources in the alloy, especially at elevated temperatures.

As we know, the mobility of solution atoms will be much higher than that of dislocations, with the result that they will not restrict dislocation motion efficiently when temperature is higher than $0.5T_m$ [13]. But in the case of the alloy in T4 state, the strength decline slowly from room temperature to 300 °C ($0.64T_m$), which can be explained by the LPSO strengthening mechanism discussed previously.

In summary, it is rational to believe that the solid solution strengthening, the β′ precipitates strengthening and the LPSO strengthening, which include the strengthening contribution of the 18R-type LPSO $Mg_{12}YZn$ phases at the grain boundaries and the strengthening contribution of the 6H′-type LPSO phases in the grain interiors, are all effective strengthening sources for WGZ1152 alloy. Because of all these strengthening sources, the alloy in T6 state exhibits high strength at both room and elevated temperatures, up to 300 °C ($0.64T_m$). The anomalous positive temperature dependence of the strength in the alloy in F and T6 state may due to the improvements of ductility and release of the stress concentration at high temperatures. Detailed experimental work is now in progress to analyze the exact mechanism.

5. Conclusions

(1) After the solution treatment, almost all the $Mg_{24}(GdYZn)_5$ eutectic phases dissolved into the α-Mg matrix, while the cuboid-shaped and RE enriched phases appeared. The mean diameter and volume fraction of the cuboid-shaped phases remained stable during the subsequent ageing. The fine dispersed β′ phase is the main precipitate in the alloy in T6 state (aged at 225 °C for 24 h), while aged at 300 °C for the same time, the coarse β precipitate becomes the major one. The two types of the LPSO phases in the WGZ1152 alloy are thermally stable, much harder than the α-Mg matrix and have a high volume fraction.

(2) Slip line observations suggest a transition from basal to non-basal slip with increasing temperature. At lower temperatures (≤100 °C), basal slip is dominant. Non-basal slip and cross slip are activated at moderate temperatures (∼250 °C), while extensive multiple slip occurs at higher temperature of 300 °C.

(3) The peak-aged alloy (T6 state) exhibits a high ultimate tensile strength of 307 ± 6 MPa and elongation to failure of 1.4 ± 0.3% at room temperature, and can maintain its strength of more than 260 MPa up to 300 °C ($0.64T_m$).

(4) The solid solution strengthening, the β′ precipitates strengthening and the LPSO strengthening, which include the strengthening contribution of the 18R-type LPSO $Mg_{12}YZn$ phases at the grain boundaries and the strengthening contribution of the 6H′-type LPSO phases in the grain interiors, are all effective strengthening sources for WGZ1152 alloy at both room and elevated temperatures.

Acknowledgements

This work was supported by the National Natural Science Foundation of China (N0. 51074106), Key Hi-Tech Research and Development Program of China (2009AA033501), National Key Technology R & D Program of China (2006BAE04B01-2) and International Cooperation Fund of Shanghai Science and Technology Committee, Shanghai/Rhone-Alpes Science and Technology cooperation fund (No.06SR07104).

References

[1] B.L. Mordike, K.U. Kainer, Magnesium Alloys and Their Applications, Wiley, New York, 2000.
[2] E. Aghion, B. Bronfin, F. Von Buch, et al., JOM 55 (2003) A30–A33.
[3] A.A. Luo, Int. Mater. Rev. 49 (2004) 13–30.
[4] C.J. Boehlert, K. Knittel, Mater. Sci. Eng. A 417 (2006) 315–321.
[5] I.A. Anyanwu, S. Kamado, Y. Kojima, Mater. Trans. 42 (2001) 1206–1211.
[6] S.M. He, X.Q. Zeng, L.M. Peng, et al., J. Alloys Compd. 427 (2007) 316–323.
[7] E. Abe, Y. Kawamura, K. Hayashi, et al., Acta Mater. 50 (2002) 3845–3857.
[8] Y. Gao, Q.D. Wang, J.H. Gu, et al., J. Alloys Compd. 477 (2009) 374–378.
[9] Y. Chino, M. Mabuchi, S. Hagiwara, et al., Scripta Mater. 51 (2004) 711–714.
[10] M. Matsuda, S. Ando, M. Nishida, Mater. Trans. 46 (2005) 361–364.
[11] T. Itoi, T. Seimiya, Y. Kawamura, et al., Scripta Mater. 51 (2004) 107–111.
[12] C.J. Chen, Q.D. Wang, D.D. Yin, J. Alloys Compd. 487 (2009) 560–563.
[13] M.A. Meyers, K.K. Chawla, Mechanical Behavior of Materials, Cambridge University Press, 2009.
[14] D.B. Williams, C.B. Carter, Transmission Electron Microscopy: A Textbook for Materials Science, Springer, 1996.
[15] Z.P. Luo, S.Q. Zhang, J. Mater. Sci. Lett. 19 (2000) 813–815.
[16] L. Zhiping, Z. Shaoqing, T. Yali, et al., J. Alloys Compd. 209 (1994) 275–278.
[17] J.F. Nie, B.C. Muddle, Acta Mater. 48 (2000) 1691–1703.
[18] S.M. He, X.Q. Zeng, L.M. Peng, et al., J. Alloys Compd. 421 (2006) 309–313.
[19] S.S. Vagarali, T.G. Langdon, Acta Metall. 29 (1981) 1969–1982.
[20] Y. Gao, Q.D. Wang, J.H. Gu, et al., Mater. Sci. Eng. A 459 (2007) 117–123.
[21] Y. Gao, Q.D. Wang, J.H. Gu, et al., J. Rare Earth 26 (2008) 298–302.
[22] D.Q. Li, Q.D. Wang, W.J. Ding, Mater. Sci. Eng. A 428 (2006) 295–300.
[23] J.F. Nie, Scripta Mater. 48 (2003) 1009–1015.
[24] J.H. Westbrook, R.L. Fleischer, Crystal Structures in Intermetallic Compounds, John Wiley & Sons, LTD, England, 1992.